Distortion Representation of Forecast Errors for Model Skill Assessment and Objective Analysis[1] Technical Report[2]

Ross N. Hoffman, Thomas Nehrkorn and Christopher Grassotti[3]
Atmospheric and Environmental Research, Inc.[4]

Revision : 1.12[5]

August 15, 1997

·

[4]Atmospheric and Environmental Research (AER), Inc., 840 Memorial Drive, Cambridge, MA 02139-3794. Phone: +1 617 547 6207. Fax: +1 617 661 6479. Net: http://www.aer.com/.

1   Introduction

We proposed a novel characterization of errors for numerical weather predictions. In its simplest form we decompose the error into a part attributable to phase errors and a remainder. The phase error is represented in the same fashion as a velocity field and is required to vary slowly and smoothly with position. A general distortion representation allows for the displacement and amplification or bias correction of forecast anomalies.

Characterizing and decomposing forecast error in this way has two important applications, which we term the assessment application and the objective analysis application. For the assessment application, our approach results in new objective measures of forecast skill which are more in line with subjective measures of forecast skill and which are useful in validating models and diagnosing their shortcomings. With regard to the objective analysis application, meteorological analysis schemes balance forecast error and observational error to obtain an optimal analysis. Presently, representations of the error covariance matrix used to measure the forecast error are severely limited. For the objective analysis application our approach will improve analyses by providing a more realistic measure of the forecast error. We expect, *a priori*, that our approach should greatly improve the utility of remotely sensed data which have relatively high horizontal resolution, but which are indirectly related to the conventional atmospheric variables.

In this project we are initially focusing on the assessment application, restricted to a realistic but univariate 2–dimensional situation. Specifically we study the forecast errors of the sea level pressure (SLP) and 500 hPa geopotential height fields for forecasts of the short and medium range. Since the forecasts are generated by the GEOS (Goddard Earth Observing System) data assimilation system with and without ERS 1 scatterometer data, these preliminary studies serve several purposes. They (1) provide a testbed for the use of the distortion representation of forecast errors, (2) act as one means of validating the GEOS data assimilation system and (3) help to describe the impact of the ERS 1 scatterometer data.

2   Data

Forecasts and verifying analyses made with the GEOS data assimilation and forecast system (Schubert *et al.* 1993 [11]) are used here. The particular experiments studied here are described by Atlas *et al.* (1995 [1]) in a study of the impact of ERS–1 scatterometer data on numerical weather prediction. The period of study is March, 1993. The forecast model and data assimilation system used in these experiments are identical to the GEOS-1 system described by Schubert *et al.*, except for some minor bug fixes and the modifications necessary to utilize surface wind vectors. Thus the control forecasts in the impact study are standard GEOS forecasts. In addition to the CONTROL experiment, several using different types of scatterometer wind information are available. Our initial prototyping and sensitivity studies use only the 2 × 2.5° CONTROL forecast for the period 6–11 March 1993. In addition we have made some comparisons to the corresponding PGLA and VARGLA forecasts. In all cases the CONTROL GEOS data assimilation is used as verification. The PGLA and VARGLA forecasts use the same setup as the CONTROL forecast, but both add ERS–1

scatterometer data to the CONTROL data sets in determining the initial conditions for the forecast. In PGLA the scatterometer data is processed using the directional filtering method of Offiler (1994 [8]), while in VARGLA, the variational analysis method of Hoffman (1984 [4]) is applied to the ERS–1 σ^0 measurements.

3   Methodology

Since we require that these distortion fields vary smoothly, a spectral representation is appropriate. Determining the distortion which provides the best match is then equivalent to minimizing the misfit between the first field and a distortion of the second, with respect to the spectral coefficients of the distortion. In the present project we use a global or hemispheric domain, and spherical harmonics as basis functions.

In brief, the distortion is determined by minimizing the objective function J, by varying the displacement and bias correction fields, where

$$J = J_r + J_d + J_a.$$

The residual cost function, J_r, measures the misfit of the distorted forecast to the verifying analysis. Minimizing J_r improves the agreement between the (distorted) forecast and the analysis. The two additional penalty terms in the objective function, J_d and J_a, ensure that the final distortion produced by the minimization is relatively smooth and not too large. (The terms cost function, objective function and penalty function are used more or less interchangeably in the literature. Here, the objective function is the quantity to be minimized, a cost function measures lack of fit to data and a penalty function measures lack of fit to a constraint.) The smoothness penalty function, J_d measures the roughness of the x- and y-displacements and of the bias correction, ensuring that the distortion is large scale. The barrier penalty function, J_a, measures the magnitude of the distortion components in a way so that small distortions are not penalized, but large distortions are penalized heavily. This has the effect of setting up a barrier to the size of the distortions which are determined. These last two terms are evaluated using the spectral coefficients of the distortion.

The three terms making up J are described in the following sections. However, in our work so far, the spectral truncations used are so severe that J_d and J_a are not used in obtaining the results presented here. In our studies at the beginning of the project we found that using the barrier and smoothness penalty functions results in distortions which are smaller in magnitude, but larger in scale, and residual errors which are larger in scale and magnitude. The spectra of the original and residual forecast error, both with and without the penalty functions show that a great deal of the forecast error on the scales of the distortion is explained by the distortion and that the penalty constraints have a strong effect limiting the smallest scales in the distortion.

Note that the limits used to define J_a are found to be very useful to precondition the minimization, even in cases where J_a is not used in the functional. Simulation experiments demonstrated that if the control vector is scaled by its limiting values estimate, the true solution is quickly recovered. If the scaling is derived from the smoothing function instead, the minimization quickly fails with false convergence. For the case of uniform scaling of the

control vector, the minimization is only partially successful: the objective function is reduced only slowly, and after 100 iterations, only half of the original forecast error is explained.

3.1   Residual cost function, J_r

The residual cost function J_r measures the misfit between the distorted forecast and the verifying analysis. We denote the forecast by F, the distorted forecast by P, and the verifying analysis, or what is considered truth, by T. The cost function is evaluated over the global domain via

$$J_r = \frac{\int_\sigma (P - T)^2 d\sigma}{\int_\sigma d\sigma}.$$

where the integral is the surface integral over the global domain. The distorted forecast P is obtained from the unmodified forecast F by adding a location-dependent bias correction $B(\lambda, \theta)$ to the values displaced by the displacement vector field $\boldsymbol{D}(\lambda, \theta) = (D_u, D_v)$, where $\boldsymbol{D}$ is expressed here in terms of its zonal and meridional components, in analogy to a wind field. Thus, we may write

$$P(\lambda, \theta) = F(\lambda', \theta') + B(\lambda, \theta),$$

where the location (λ', θ') is found by following the displacement vector $\boldsymbol{D}(\lambda, \theta)$ back from its endpoint (λ, θ).

We represent the scalar field B by a truncated series of spherical harmonics, and the vector field $\boldsymbol{D}$ in terms of the spectral coefficients of the corresponding vorticity (ζ) and divergence (δ) fields. A degree of smoothness can thus easily be imposed by the truncation of the series, and further constraints can separately be imposed on the divergent and rotational parts of the displacement field. The control vector C for the optimization problem is thus composed of the spectral coefficients for B, ζ and δ:

$$C = (B, \zeta, \delta)^T.$$

Both the forecast F and the verifying analysis T are available on regular latitude-longitude grids. For evaluation of the integral, it is convenient to first interpolate T to a Gaussian latitude-longitude grid, in which case the formula for J_r takes the form

$$J_r = \sum_j \frac{w_j}{N_j} \sum_i (P_{ij} - T_{ij})^2,$$

where indices i, j denote the grid point location in longitude and latitude, N_j is the number of longitude points for latitude j (this number will depend on j only for reduced Gaussian grids), and w_j is the Gaussian weight for latitude j. These weights are normalized such that their sum over all latitudes is unity.

The first step in the evaluation of the P_{ij} requires the spectral transformation from C to B_{ij} and $(D_u, D_v)_{ij}$. The next step is the evaluation of $F(\lambda', \theta')$. Following Ritchie (1987 [9]), we define latitude-longitude points in terms of 3-dimensional cartesian vectors centered on the unit sphere. The origin point (λ', θ'), corresponding to the 3-dimensional cartesian vector $\boldsymbol{r}$, is then found in the plane of the endpoint location vector $\boldsymbol{g}$ (corresponding to gridpoint (λ_i, θ_j)), and the displacement vector $\boldsymbol{d}$ (corresponding to $(D_u, D_v)_{ij}$):

$$\boldsymbol{r} = \alpha \boldsymbol{g} + \beta \boldsymbol{d},$$

where the coefficients α and β are chosen to satisfy the constraint that r must lie on the surface of the sphere, and that the length of the displacement vector d is equal to the great circle distance between g and $\dot{r}$. Finally, the value $F(\lambda', \theta')$ must be obtained by bilinear interpolation in longitude and latitude from the surrounding grid point values.

3.2   Smoothness penalty function, J_d

The smoothness penalty function, J_d is given by a simple quadratic form in terms of the spectral coefficients of the distortion,

$$J_d = \Sigma_j w_j C_j^2, \tag{1}$$

where j ranges over the ordering of the spectral wavenumber vectors, k, and over the components of the distortion—B, ζ, δ. Different specifications of w_j are under study. For example, consider the part of J_d due to the bias correction. In continuous form this is given by,

$$J_{d,B} = \frac{1}{\sigma_B^2} \int \int (\nabla^{2\nu} B)^2.$$

Here ν is an adjustable parameter normally taken to be 1 and σ_B is the scale for B. Larger values of ν result in greater smoothing by emphasizing the contributions of higher wavenumbers to J_d. Using the spectral representation of B, the orthonormality of the spherical harmonics $\Psi_n{}^m$, and the eigenstructure $\nabla^2 \Psi_n{}^m = -n(n+1)\Psi_n{}^m$, we find that,

$$w_{k,B} = (n_k(n_k + 1))^{2\nu}/\sigma_B^2.$$

3.3   Barrier penalty function, J_a

The functional J_a serves to limit the amplitude of the distortion. For efficiency the limits are set on the spectral coefficients. These limits are chosen in such a way that the grid point (or physical space) values of bias and displacement at all locations will be limited by specified values. In addition the spectral coefficient limits provide a good scaling (or conditioning) for the minimization. Test runs using synthetic data indicate that convergence of the minimization is sensitive to the scaling of the control vector.

The form of J_a is chosen to be,

$$J_a = \Sigma_j (C_j/S_j)^{2\mu},$$

where S_j are the spectral limiting values for the C_j. The adjustable parameter μ, nominally 10, controls the steepness of the barrier in spectral space (Fig. 1).

There is no unique way of setting the spectral limits. We choose limits which correspond to an equipartitioning, among the spectral modes, of the contributions to the physical space bias correction or displacement component. Here mode means each pair (m, n). The reasoning for this is that no matter what the signs of the spectral coefficients, the modes will tend to add up somewhere in the physical domain. On the other hand, the contributions within a particular mode, for example due to the sine and cosine components, are always out of phase and therefore add up in an *rms* sense. The limits on components are chosen to correspond to a further equipartitioning.
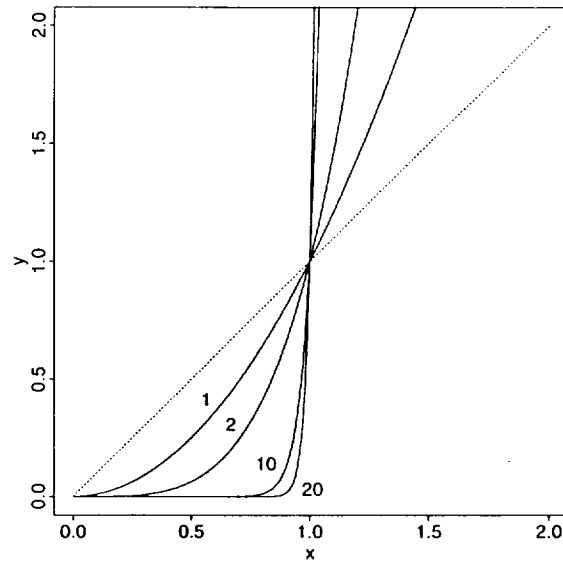
Figure 1: The component of the barrier function for a single term ($y = x^{2\mu}$ where $x = C_j/S_j$), for μ equal to 1, 2, 10, 20.

3.4 Implementation details

The algorithm is implemented in Splus and Fortran. The spectral transform and computation of Gaussian latitudes and weights use a set of general purpose Fortran library functions. All computations are performed in double precision. To minimize J we use the built-in Splus function nlminb, which implements the algorithms of Dennis et al. (1981 [3]). The nlminb algorithm uses function and gradient values. Second derivatives of the cost function are estimated by finite differences, using repeated evaluations of the gradient and cost function.

At first we used the version of the minimization algorithm which requires function values only. However, the finite difference approach is computationally inefficient, and we have recently developed the adjoint of the calculation of J. To develop the adjoint we use tools previously developed for this purpose (Hoffman et al. 1992 [6]). In addition, in the present case the spectral transforms are nearly self-adjoint (Hoffman and Nehrkorn 1989 [7]), so the amount of actual adjoint code for the transforms is limited. The adjoint calculates the gradient of the cost function very efficiently. This technique gains more than an order of magnitude decrease in computational time and provides a more accurate gradient, thereby eliminating some difficulties reported last year.

For example, in our first annual report, one concern was reproducibility. We reported that the minimization sometimes terminated immediately with a "false convergence" condition when starting from the reasonable initial estimate of zero distortion. As discussed, this is a point of maximum non-differentiability and the finite difference calculation of the gradient here is very sensitive to the step size. To avoid this problem, we set the initial estimate to random numbers. Use of random initial estimates brings with it a concern for reproducibility.

We have made two enhancement to eliminate this problem. First, we interpolate the original analysis to a new grid using Gaussian latitudes and longitudes offset by half a grid

length. Now a zero displacement corresponds to locations interior to the grid of the analysis, where the interpolation of the analysis is differentiable. Second, use of the adjoint eliminates finite difference errors.

Another concern was convergence. Now, with the efficiency of the adjoint code, we can eliminate this concern by using more than enough iterates. All results presented here use 100 iterations.

4   Results

Our results show that the methodology works, that a large part of the total error may be explained by a distortion limited to $T10$ truncation (i.e., triangular truncation at wavenumber 10), and that the remaining residual error contains mostly small spatial scales. With forecasts separated by 12 h, time continuity of the distortion fields describing the forecast errors is present in some regions, but lacking in other regions.

Experiments so far are all based on the first set of forecasts described in Section 2 for the CONTROL, PGLA and VARGLA experiments. The CONTROL experiment analyses are always used as the verification.

Initially we focused on the northern hemispheric 72 h CONTROL forecast of 500 hPa height valid at 00 UTC 9 March 1993. In the nominal case, we use $T10$ truncation and a Gaussian grid with half the resolution of the forecast fields to represent the distortion, and do not use the barrier and smoothing functions. Preliminary real data tests using $T5$ truncation were unsatisfactory and spectral analysis of the forecast and verification fields indicated that the minimum required wavenumber truncation is 10. Some of these results were reported on in our first annual technical report. More recently we have extended our work to the sea level pressure (SLP) field, and to the PGLA and VARGLA experiments for forecast ranges of 12 − 120 h.

In general, the distortion fields appear to properly account for the forecast errors. Visual examination of the distortion fields reveals a number of features with phase and amplitude errors, some of which will be discussed below. Table 1 shows that the size of the forecast errors for SLP increases with time for the CONTROL forecast and that the percentage of the squared error explained by the distortion increases from 82% to 94%. In general, both the displacements and biases increase with forecast length for the first 72 h. This is obvious in both the plots (shown for one region below) and in statistics of the solutions.

In Table 1 the statistics are calculated as follows for each run for the distortion corresponding to the initial estimate of zero distortion and to the solution. The rms error is the rms residual error for the hemisphere (in mb), calculated as the square root of J_r. The rms gradient is the rms scaled gradient (in mb^2), calculated as

$$(\sum_j (S_j \frac{\partial J}{\partial C_j})^2)^{1/2},$$

where the S_j are scales given by the limiting values defined in Section 3.3. The distortion size is the dimensionless distance in scaled phase space, calculated as

$$(\sum_j (C_j/S_j)^2)^{1/2}.$$

Table 1: Summary statistics for SLP for the CONTROL forecast every 24 h. The calculation of the statistics is described in the text.

Forecast Hour	Initial rms		Distortion Size	Final rms	
	Error	Gradient		Error	Gradient
24	2.545	3.303	11.183	1.094	0.110
48	4.506	7.480	23.509	1.787	0.153
72	6.727	10.280	30.490	2.199	0.106
96	7.672	12.333	33.173	2.295	0.121
120	9.060	17.618	29.447	2.217	0.162

In all cases 100 iterations were used by the minimization. Clearly the minimization greatly reduces the size of the gradient and the residual error.

4.1   East coast cyclogenesis

Figure 2 shows the evolution of the SLP field in the GEOS CONTROL assimilation at 24 h intervals beginning with the CONTROL initial conditions of 00 GMT 6 March 1993, for a region centered on the east coast of North America. A low forming off of New Jersey intensifies for 72 h and tracks ENE towards Iceland for the entire 120 h period. At 48 h a second low enters the domain over the Great Lakes (panel c) and follows the primary low, nearly merging with it at 120 h. This second low does not intensify during this period. Finally, a third low appears over Pennsylvania at 120 h.

By 96 h the primary low is no longer intensifying and is now positioned somewhat ahead of the upper level trough at 500 mb. The 500 mb verification and CONTROL forecast are shown in Fig. 3, (panels a and c). The second trough, with a closed low just south of the Canadian maritimes is too intense and has not moved eastward enough' in the forecast. The main feature in the error field (forecast minus analysis) is therefore an area of negative difference, extending along the eastern seaboard (e). The distorted forecast (b) is much closer to the verification (a). The residual error (f), that is the error not explained by the distortion, is not only small in magnitude, but also small in scale. The distortion (d) is shown as vectors indicating how the forecast is displaced and as a height bias which is added to the displaced forecast.

In this case, after 100 iterations, a solution for the distortion is reached which reduces the rms residual error from 74.29 m to 17.04 m, which corresponds to a 19-fold reduction in the objective function. The distortion field has significant displacements (exceeding 500 km in some locations) and bias corrections (100 m).

The minimization procedure uses all degrees of freedom available to match the distorted forecast to the verification. Thus, the differences in the secondary trough are partly explained by eastward displacement, and by a dipole in the bias field. In addition northward components of the displacement near Georgia act on the gradient of zonally averaged 500 mb height to weaken the trough in this area. Some of these distortion field features run counter to our intuitive expectations and we address possible remedies in Section 5.1.1.

At the surface at 96 h, the secondary surface low in the CONTROL forecast (Fig. 4.a) is

a

960   980   1000   1020   1040

b

960   980   1000   1020   1040

c

960   980   1000   1020   1040

d

960   980   1000   1020   1040

e

960   980   1000   1020   1040
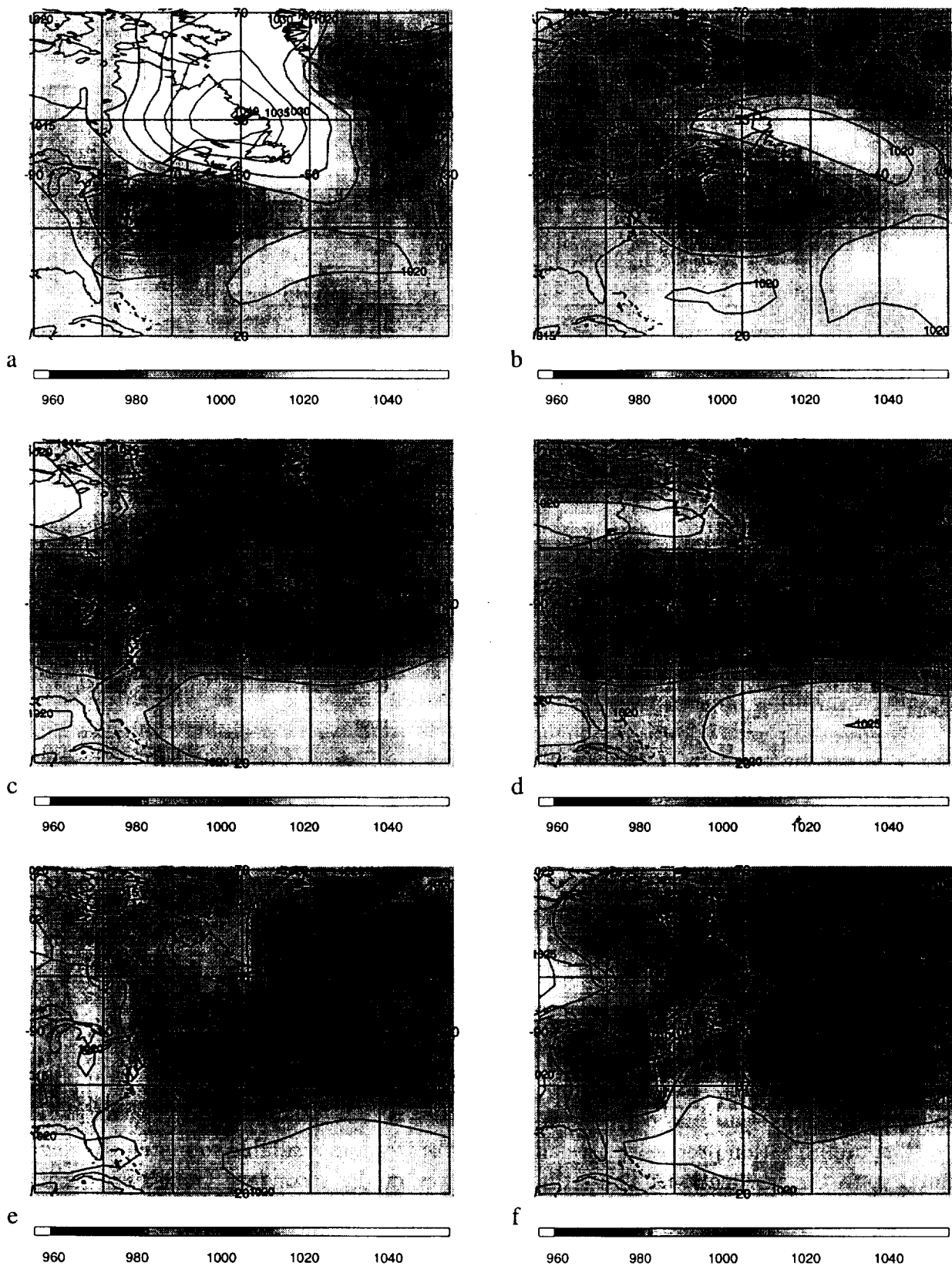
f

960   980   1000   1020   1040

Figure 2: Evolution of the SLP field in the GEOS CONTROL assimilation every 24 h starting with the initial conditions of 00 GMT 6 March 1993.
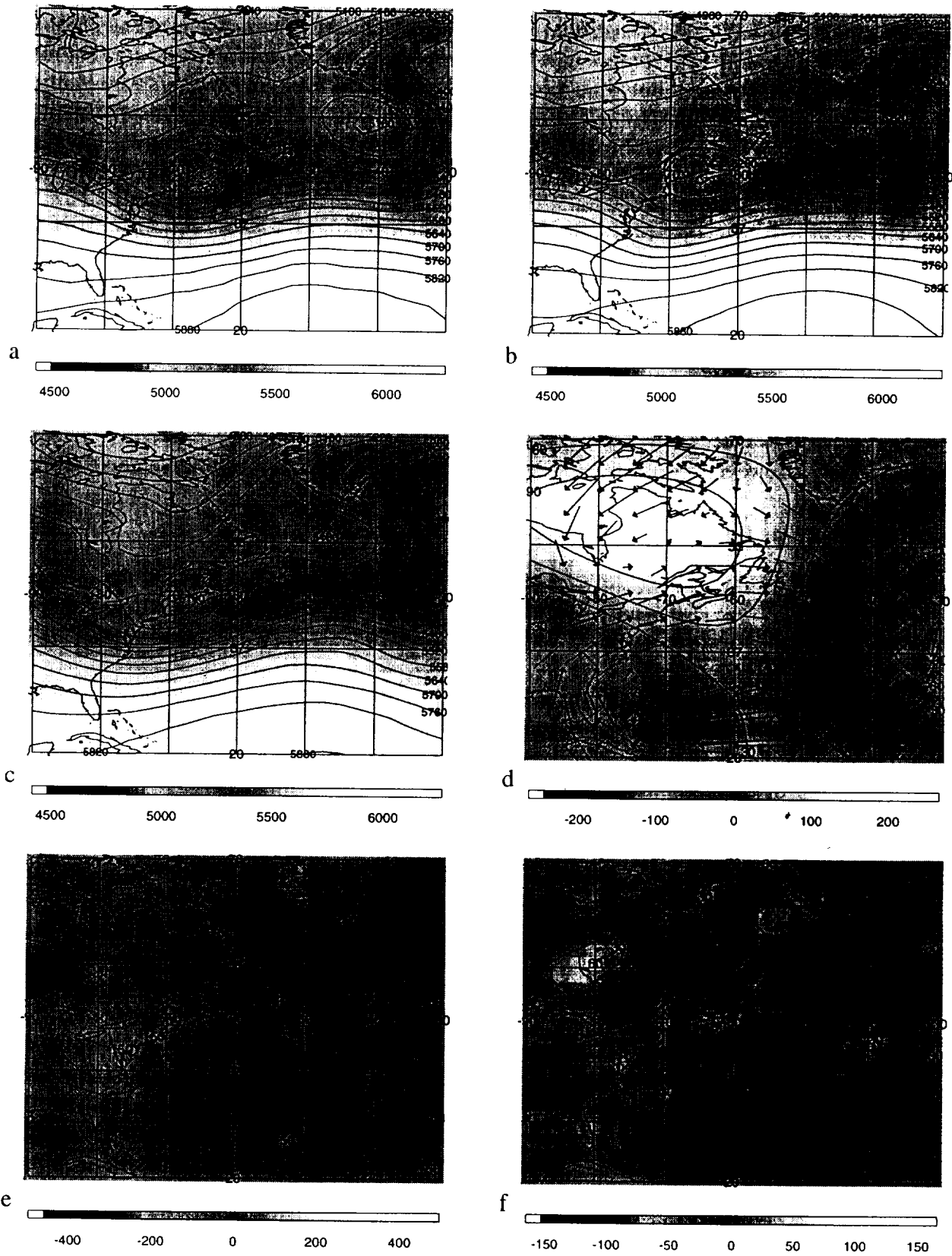
Figure 3: The 96 *h* 500 *mb* verification (a), distorted forecast (b), CONTROL forecast (c), distortion (d), forecast error (e), and residual error (f). All valid 00 GMT 10 March 1993.

stronger and positioned westward relative to verification. At Boston for example, the wind would be stronger and with a more northerly component. The primary low is approximately correct in terms of strength but is postioned northwest of the verifying low by several hundred kilometers. The distortion (b) in this case has significant southeastward displacements in the area of the primary low. In the area of the secondary low eastward displacements are combined with positive bias corrections. The distortion for SLP is quite different from the distortion for 500 *mb*.

The other panels in Fig. 4 show the forecasts and distortions for the PGLA and VARGLA experiments. In PGLA, the two forecast lows are very similar to the CONTROL case, and the distortions in these areas are similar. In VARGLA, the secondary low is weaker and more in agreement with the verification. Note that for the region plotted, the VARGLA distortion is larger, and the residual error is smaller.

Interestingly, all three forecasts show evidence of a strong front in the SLP field near 32W. In the CONTROL forecast this feature is oriented very nearly North-South, while in both experiments with ERS-1 data, this front curves towards the west as one moves away from the low. However, verification (Fig. 2.e) shows only a hint of a front in this location.

4.2   Central Pacific Ocean

We now focus on the region of the North Pacific Ocean near the dateline where more than one "best" distortion is a potential solution due to the extreme differences in features between the forecasts and the analyses; this results in poor time continuity of the resulting distortion fields.

Figs. 5 thru 9 contain the verification, forecast, forecast error, distortion, and residual error fields, respectively for the 72 − 120 *h* (day 3-5) forecasts. In each of the figures, the left hand panels (a,c,e) contain the sea level pressure fields, and the right hand panels (b,d,f) contain those for the 500 *mb* height fields.

First we compare the 500 *mb* height verification and forecast fields. On day 3 we see that the verification shows two troughs, each with closed circulations, at 40N, 153E and 40N, 205E, respectively, separated by a broad ridge. The other important feature is another trough at 50-55N and 170E, just east of the Kamchatka peninsula. The corresponding forecast contains these features, but in a very different orientation. The easternmost trough is greatly underforecast in intensity, and is seen only as a weak shortwave in the flow. The western trough is also much weaker, and is located too far west, while the northern trough is too strong and is positioned too far south and east, effectively eliminating the broad ridge seen in the verification. By the day 4 and 5 (96 *h* and 120 *h*) time period the evolution of these features in the forecast and verification maps diverges greatly. The western trough intensifies into a major system while migrating northeastward. In response the ridge ahead of this system sharpens and increases in amplitude. To the east the northern and southern troughs coalesce at 210E. In contrast, the forecast field weakens the western trough, propagates the weaker eastern shortwave out of the plot region, and incorrectly amplifies and slows down the northern shortwave. The result is that by 120 *h*, the forecast and verification fields are essentially one-half a synoptic wavelength out of phase with one another between 165E and 210E. This can be seen in the strong tripole pattern in the forecast error fields (Fig. 7) The sea level pressure fields in this case are basically a reflection of the upper level fields and
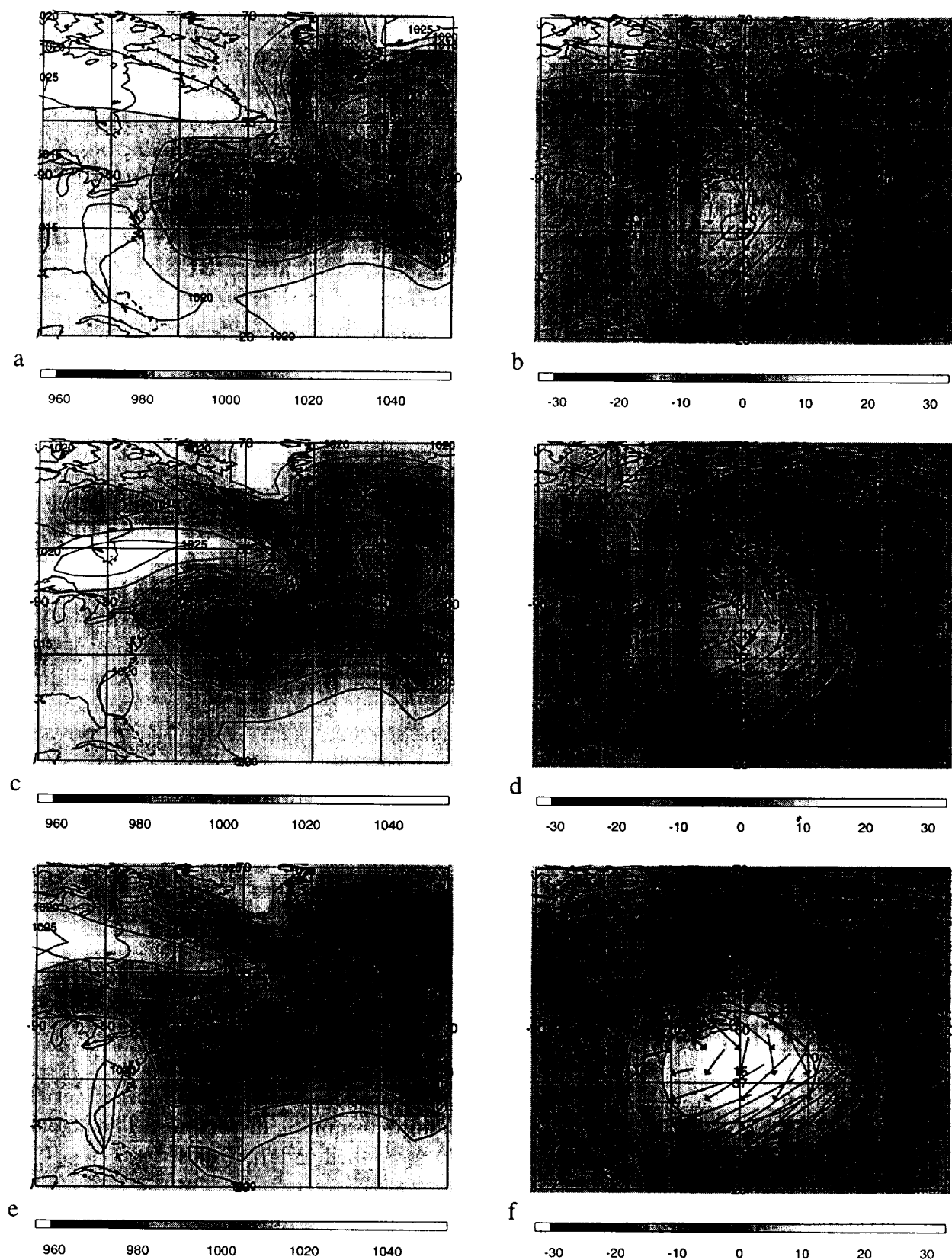
Figure 4: Impact of ERS–1 data on the 96 h SLP field. The left column shows the CONTROL, PGLA and VARGLA forecasts from top to bottom and the right column shows the corresponding distortions. All valid 00 GMT 10 March 1993.

show the same relative errors.

The patterns of the distortion fields show only limited temporal continuity, and this may be due to the degree of misphasing between the forecast and verification features. This is particularly true for the 500 mb height field distortions (Fig. 8.b,d,f). On day 3 the distortion shows a large region of negative bias corrections in the center of the domain, possibly in response to the two large positive forecast error centers associated with the eastern and western troughs. With a higher spectral truncation, the algorithm may have been able to resolve these into two distinct features. The displacement field shows a strong northward component as it attempts to build the ridge seen in the verification. By days 4 and 5 the bias correction fields have split somewhat into two centers, but they are not sharply-defined. The displacement field on day 4 bears little resemblance to that on either day 3 or on day 5. Since the features in the forecast evolve into a configuration so different from that of the verification there is no clearly "correct" displacement. This is consistent with our original assumption that the technique requires similar features in both forecast and verification maps in order to be effective. Nevertheless, the residual errors (Fig. 9.b,d,f) show that the algorithm has still reduced the forecast error.

The sea level pressure distortions (Fig. 8.a,c,e) are somewhat more consistent in time, and with the features seen in the error plots. The bias corrections show two centers of negative values whose location and temporal evolution correspond to those in the forecast error plots. The displacements in days 4 and 5 are consistent with one another, with a large area of strong westward displacements. However, since the forecast and verification features are so out of phase, these displacements are not very representative of the actual displacement errors, even though they are again successful at reducing the forecast error, as seen in the residual error fields (Fig. 9.a,c,e).

Figs. 10 and 11 show the day 5 distortions and corresponding forecast fields for the CONTROL, PGLA, and VARGLA experiments. In general, the distortions are qualitatively similar from one experiment to another. The only exception is the sea level pressure displacement field for the PGLA experiment. One important characteristic of the plots in general is that the distortions of the pressure and height fields are often quite different from one another. While this is not critical for the so-called assessment application of forecast errors, it is important for potential use of the analysis application, when model fields may be changed, prior to or as part of an objective analysis procedure.

5   Plans for future work

We have accomplished a lot in short order, but much remains to be done. In broad terms we have developed and tested an efficient algorithm for determining distortions. The algorithm and constraints must now be tested and tuned, and applied to larger data sets.

5.1   FY97 (the current contract)

Our immediate plans to extend the current research fall into several related subtopics, as described in the following paragraphs.
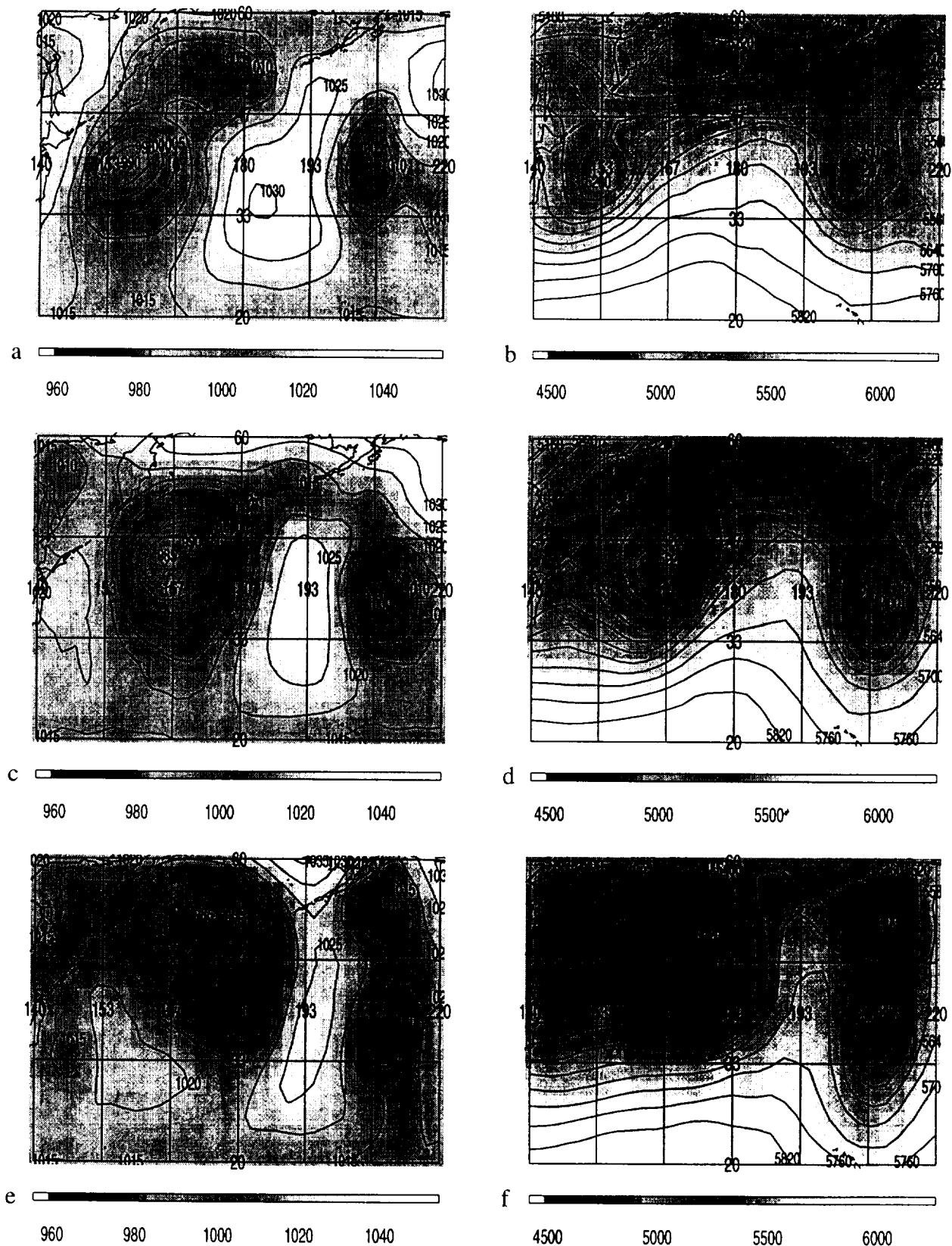
Figure 5: Verification fields for 72 h, 96 h, 120 h (forecast days 3-5), top to bottom. Left column shows the verification fields for SLP and the right column shows the verification fields for 500 mb height.
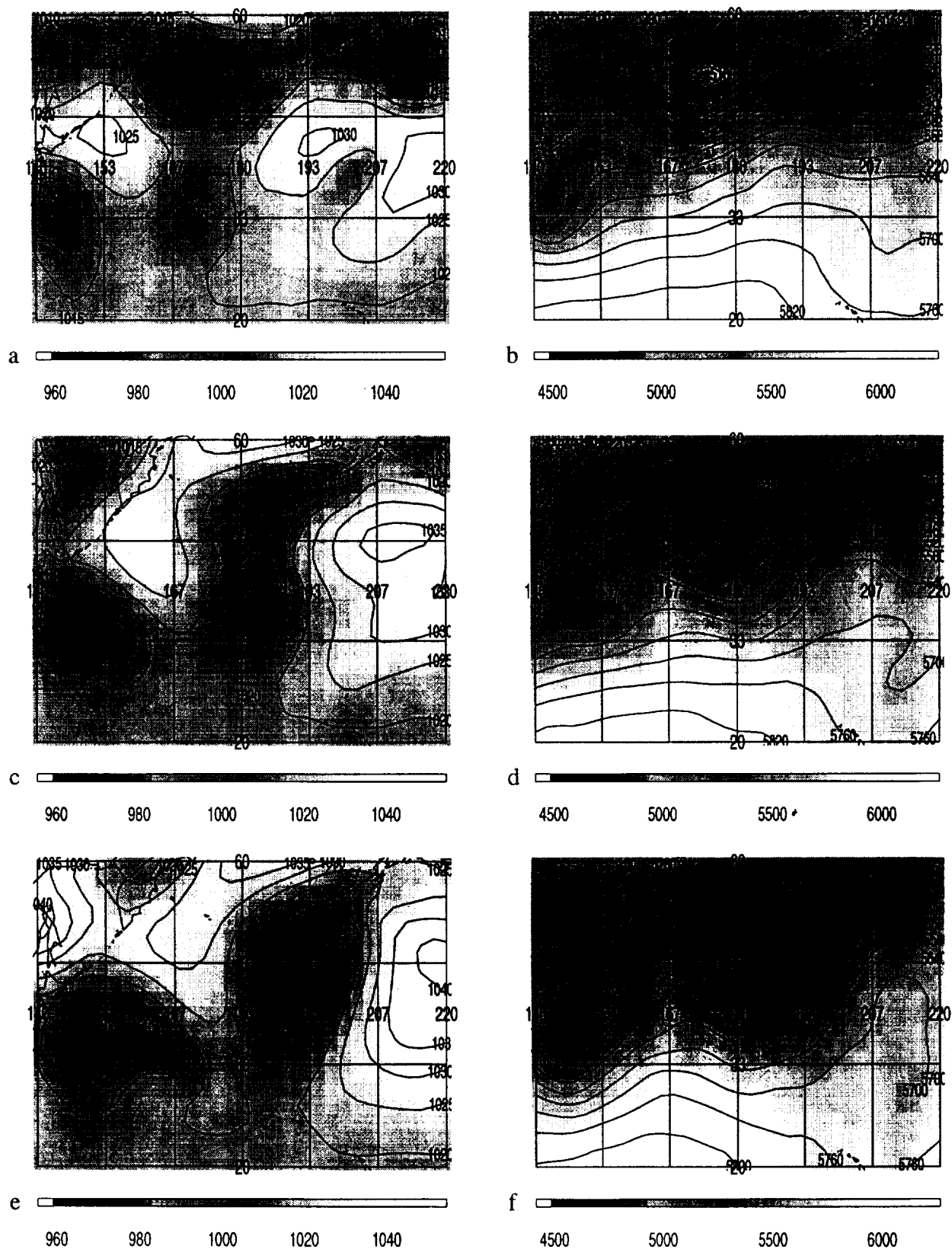
Figure 6: Forecast fields for 72 h, 96 h, 120 h (forecast days 3-5), top to bottom, for the CONTROL experiment. Left column shows the forecast fields for SLP and the right column shows the forecast fields for 500 mb height.
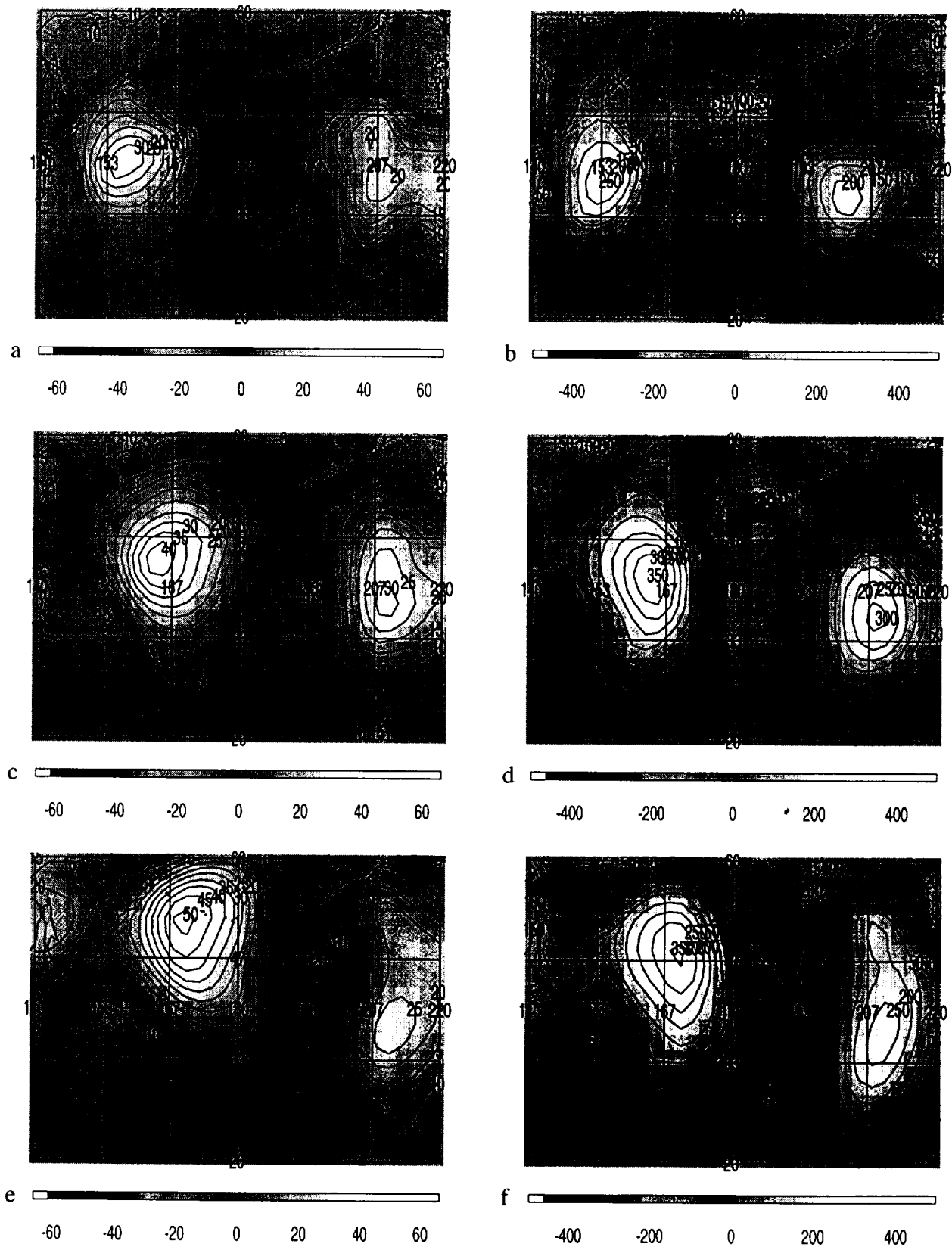
Figure 7: Forecast error fields for 72 h, 96 h, 120 h (forecast days 3-5), top to bottom, for the CONTROL experiment. Left column shows the forecast error for SLP and the right column shows the forecast error for 500 mb height.
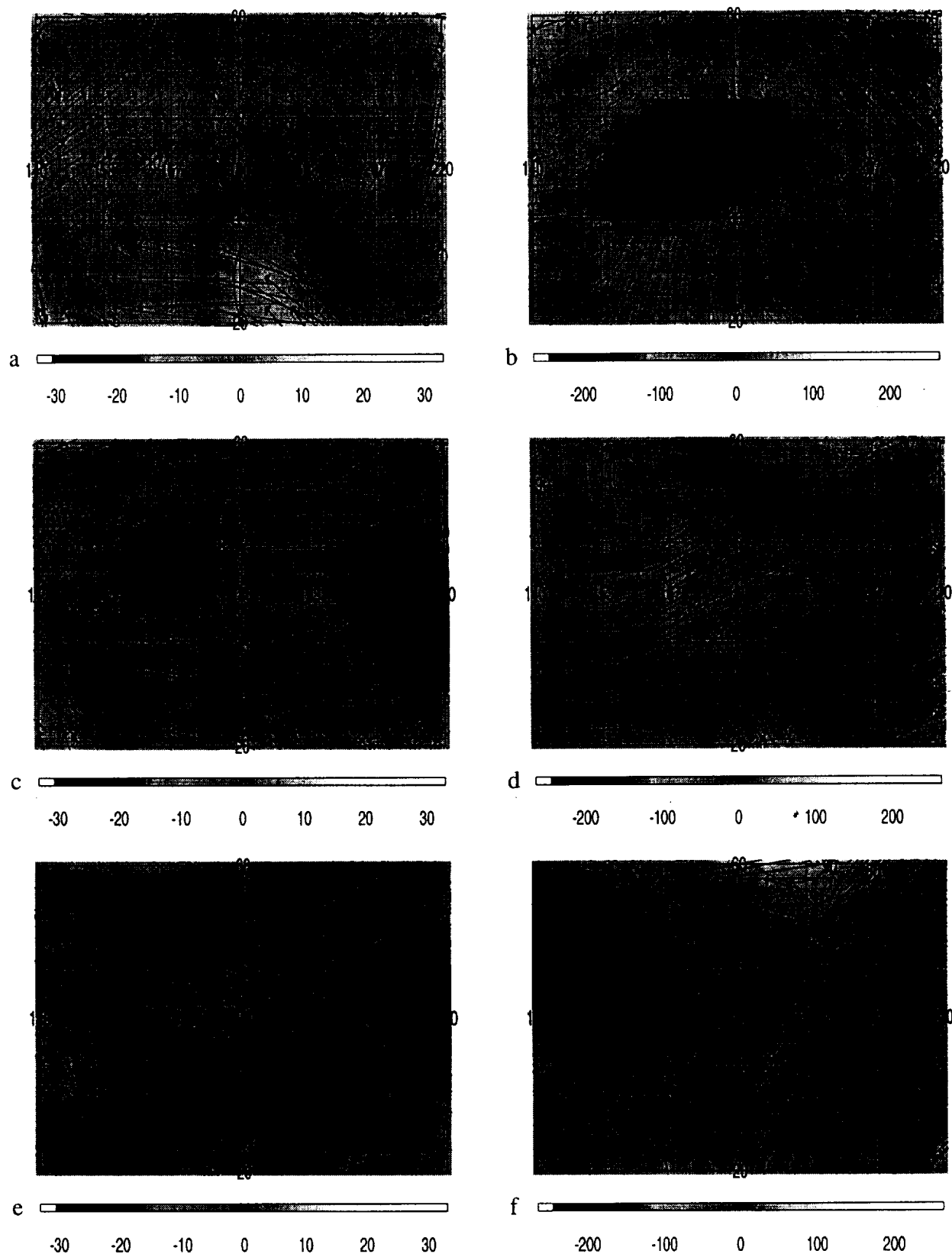
Figure 8: Distortion fields for 72 h, 96 h, 120 h (forecast days 3-5), top to bottom, for the CONTROL experiment. Left column shows the distortion for SLP and the right column shows the distortion for 500 mb height.
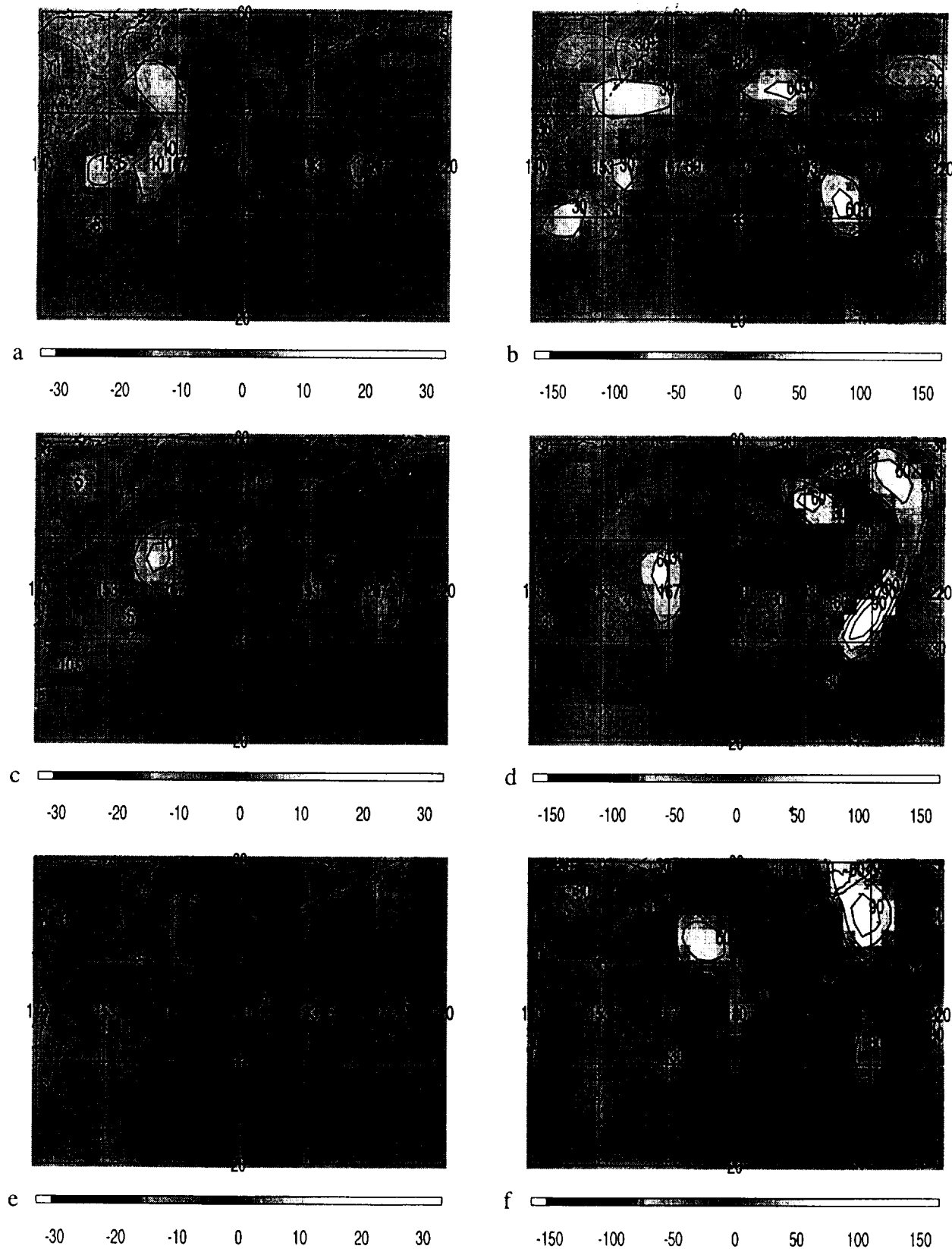
Figure 9: Residual error fields for 72 *h*, 96 *h*, 120 *h* (forecast days 3-5), top to bottom, for the CONTROL experiment. Left column shows residual error for SLP and the right column shows residual error for 500 *mb* height.
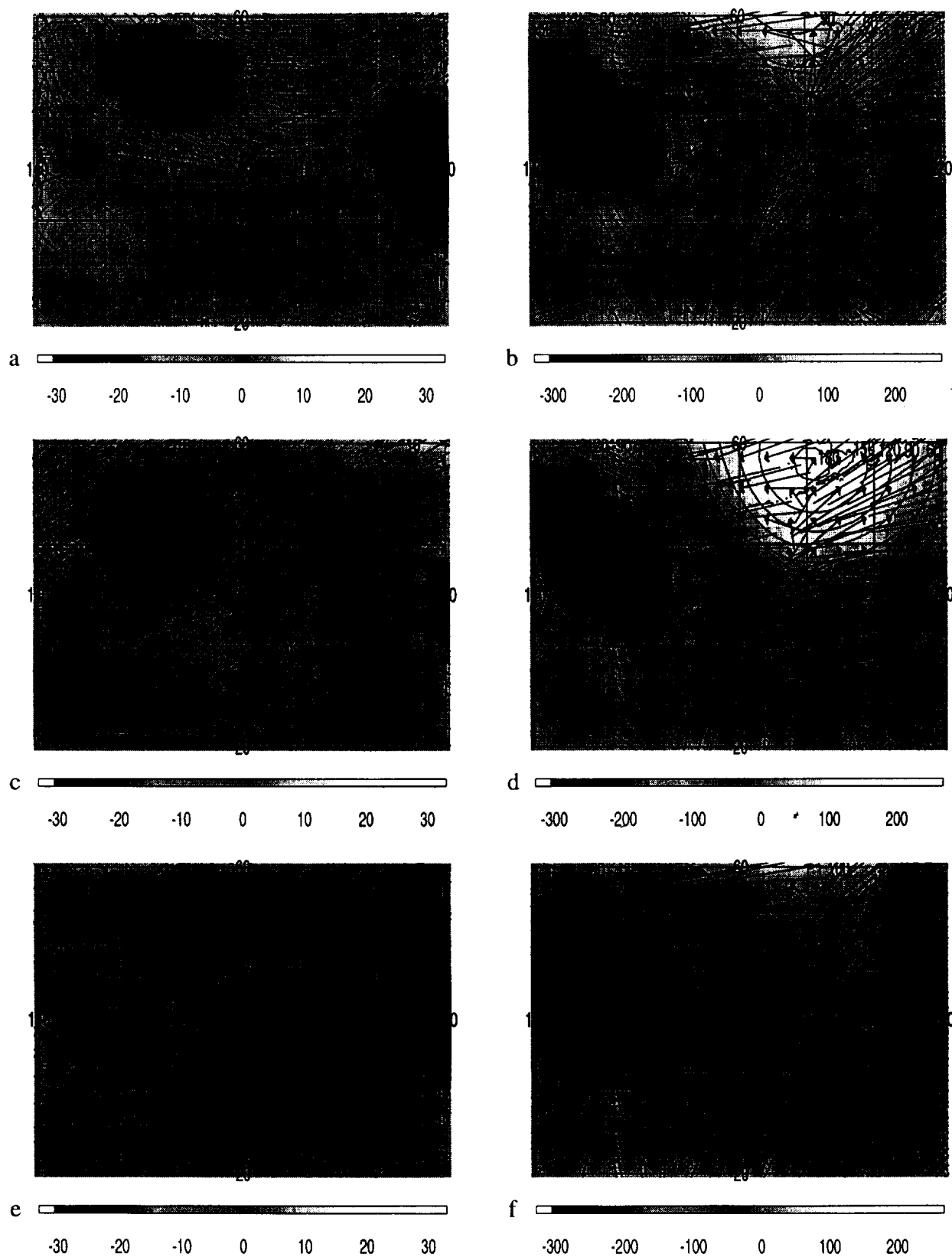
Figure 10: Distortion fields for the 120 *h* (day 5) forecast. Results for CONTROL, PGLA, and VARGLA experiments are shown from top to bottom. Left column shows results for SLP and right column shows results for 500 *mb* height.
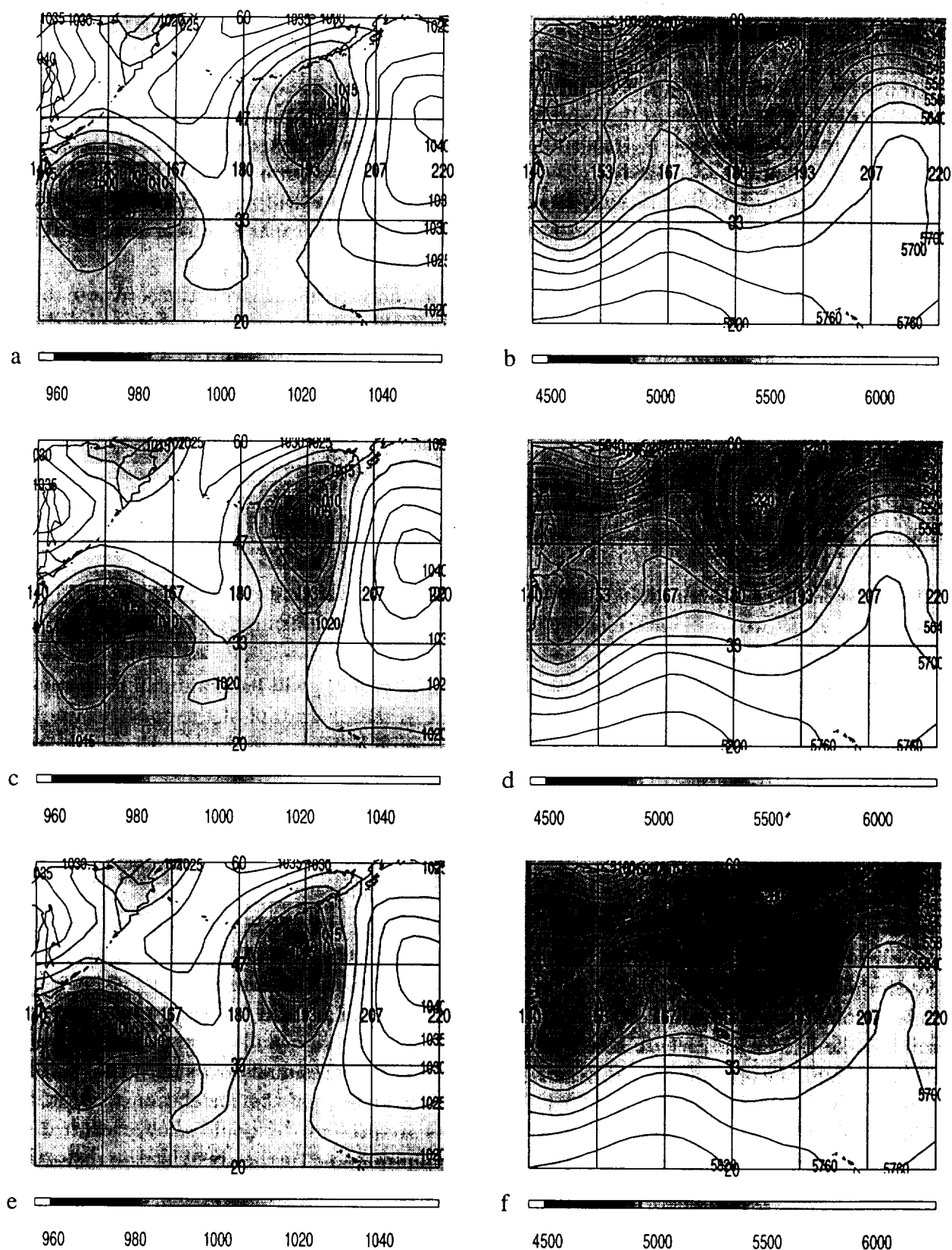
Figure 11: Forecast fields for the 120 *h* (day 5) forecast. Results for CONTROL, PGLA, and VARGLA experiments are shown from top to bottom. Left column shows results for SLP and right column shows results for 500 *mb* height.

5.1.1   More cases and variables

The analyses will be extended to other cases in the suite of experiments. So far we have used only the Control and PGLA and VARGLA runs for 6 March. We have access to cases for 6, 11, 16 and 21 March for Control, ESA, PNMC, and PGLA experiments. A complete evaluation of the errors of all these experiments would constitute a major study. However at least the other CONTROL forecasts will be analyzed. We will also examine some of the Southern Hemisphere results since we know that significant impacts of scatterometer data exist there.

Fields besides SLP and 500 mb height could be analyzed using distortions. Anomalies of SLP and 500 mb height from the zonally averaged climate mean and potential vorticity should provide distortions more in line with intuitive expectation. We will also experiment with some displacement only distortions. We will also examine differences between the current approach and determining first the displacement and then the bias correction, holding the displacement fixed.

5.1.2   Parameter sensitivity studies

We will examine the sensitivity of the distortion and error fields to the parameters of the method $\nu, \sigma_d, \sigma_A, \nu_a, \mu$. The use of different spectral truncations and grid resolutions will be studied.

Different ways of setting the spectral limits and/or scales will be explored. In particular, we will try to eliminate some of the assumptions in the derivation of the spectral limits by using the actual maximum amplitudes of the expansion functions evaluated on the transform grid.

5.1.3   Refining J_d

We will experiment with different functional forms of J_d. For the simple measures of the magnitude of the distortion and the lack of smoothness of the distortion, which are discussed by Hoffman *et al.* (1995 [5]), J_d takes the form of Equation 1, where the weights w_j depend only the total wave number n. Several different forms for w_j will be tried. For example we might take $w_j = \alpha n^{2\beta}$, where β is a small integer and where α and β are to be determined. To determine the optimal values we will cross-correlate the residual errors with the distortion errors at various displacements. For this purpose we will vary the correlation window from 500 to 1000 to 2000 km. If significant correlations are present we should allow greater distortions. If no significant correlations remain, we should try to further restrict the distortions. These ideas will be tested in parallel with synthetic data for the same versions of J_d.

We have so far examined distortions with no constaints other than spectral truncation. The use of constaints like J_d and the choice of which variable to apply the distortion to must be explored. Differences in the distortion fields for different forecast fields should be examined in more detail.

5.1.4   Time continuity

To investigate the time continuity of the distortions we examined forecasts every 12 h, for the CONTROL case of 6 March 1993. The time continuity of the distortion during the course of the forecast is good in some areas and involves large changes in other areas.

Methods to enforce consistency in the evolution of the distortion must be developed. Consistency is most lacking if a feature in the forecast may be explained in terms of more than one feature in the verification. These situations are very sensitive to initial estimates of the distortion and the parameters of the algorithm. The use of J_d and better initial estimates are expected to be helpful here. Also constaints like J_d might be applied to 12 or 24 h changes in the distortion.

For example, experiments will test the suitability of extrapolating distortions in time to provide initial estimates for the minimization. The initial estimate of the 72 h distortion might be taken to be $1.5C_{48\ h}$ or $2C_{48\ h} - C_{24\ h}$. This may also improve efficiency.

5.1.5   Use of the 6.7 μm water vapor imagery

The second set of our proposed experiments compare satellite data—in this case geostationary 6.7 μm water vapor imagery—to a background field calculated from a short term forecast. The 6.7 μm water vapor imagery data are ideal for our study since they have striking patterns and features, which can be matched by corresponding patterns and features in the short term forecast. Additionally geostationary water vapor data are available with high temporal frequency and near global coverage. However, we will begin our investigation with VAS data only, since the METEOSAT sensors do not have on-board calibration. (See Schmetz and Turpeinen (1988 [10]) for a discussion of the calibration of these data.)

The approach for this task will be similar to that taken for the 500 hPa height fields. In this case, we take the short term forecast of the 6.7 μm water vapor imagery as X_f and the observed imagery as X_a. There are two complications: the calculation 6f the simulated 6.7 μm water vapor imagery, which is discussed in the next paragraph, and the need to quality control the observed imagery. Quality control is required because of limited coverage, missing data, and the difficulty of simulating the 6.7 μm water vapor imagery at large incidence angles, over high terrain for dry conditions, and in the presence of cloud. It will be necessary, at least initially, to resample the imagery to a relatively coarse regular grid. Then we will determine smooth displacement and amplification fields needed to best match the forecast and imagery. The algorithm needed here is identical to that used for the 500 hPa height fields. The resulting fields of displacement and amplification provide a correction to the short term forecast.

We will simulate the 6.7 μm water vapor imagery from the forecast values of temperature and humidity using a standard radiative tranfer model (RTM). The simulated 6.7 μm water vapor imagery will then be held fixed in determining the distortion. Changes in incidence angle related to displacements on scales of 100 km are $O(1°)$. The sensitivity of the calculated brightness temperature to incidence angle is small (Fig. 12) and will be assumed negligible in these calculations. The RTM used in Fig. 12, and a candidate for future calculations is MODTRAN. Although MODTRAN is inefficient, it is accurate and well documented (Berk *et al.* 1989 [2]).
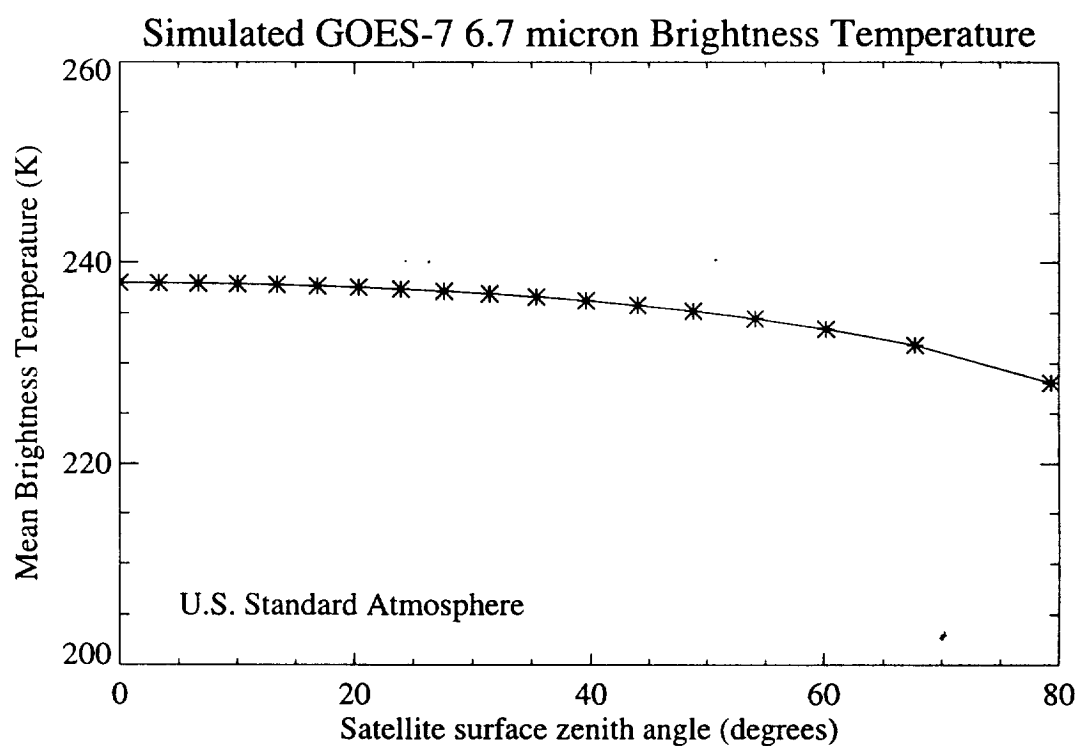
Simulated GOES-7 6.7 micron Brightness Temperature

Figure 12: Variation of 6.7 μm brightness temperature with incidence angle for the U.S. standard atmosphere.

5.2 FY98 - FY00

We have already submitted a proposal for a continuation of this project. We propose to demonstrate the usefulness of the distortion representation of forecast errors by conducting realistic studies of the assessment application and the objective analysis application. For the assessment application we will continue to study forecast errors of the 500 hPa geopotential height field for forecasts of the short and medium range. The forecasts and analyses which will be used are realistic quasi-operational forecasts. A preliminary to this task is to test and tune EOF representations of the distortions, using the results of the current project for the March 1993 forecasts. For the objective analysis application, we will apply the 6.7 μm water vapor imagery to determine short term forecast errors, as a standalone objective analysis application. These tasks are described in our proposal submitted 20 June 1997.

References

[1] R. Atlas, R. N. Hoffman, E. Brin, and P. M. Woiceshyn. The impact of ERS-1 scatterometer data on GEOS model forecasts. In *International Symposium on Assimilation of Observations in Meteorology and Oceanography*, Tokyo, Japan, 13-17 Mar. 1995. WMO.

[2] A. Berk, L. S. Berstein, and D. C. Robertson. MODTRAN: A moderate resolution model for LOWTRAN 7. Technical Report 89-0122, Air Force Geophysics Laboratory, Hanscom AFB, MA, 1989.

[3] J. E. Dennis, D. M. Gay, and R. E. Welsch. An adaptive nonlinear least-squares algorithm. *ACM Transactions on Mathematical Software*, 7:348-383, 1981.

[4] R. N. Hoffman. SASS wind ambiguity removal by direct minimization. II: Use of smoothness and dynamical constraints. *Mon. Weather Rev.*, 112:1829-1852, 1984.

[5] R. N. Hoffman, Z. Liu, J.-F. Louis, and C. Grassotti. Distortion representation of forecast errors. *Mon. Weather Rev.*, 123(9):2758-2770, Sept. 1995.

[6] R. N. Hoffman, J.-F. Louis, and T. Nehrkorn. A simplified view of adjoint calculations in the discrete case. Technical Memorandum 184, Eur. Cent. for Med. Range Weather Forecasts, Reading, England, 1992.

[7] R. N. Hoffman and T. Nehrkorn. A simulation test of three-dimensional retrievals. *Mon. Weather Rev.*, 117:473-494, 1989.

[8] D. Offiler. The calibration of *ERS-1* satellite scatterometer winds. *J. Atmospheric Oceanic Technology*, 11(4):1002-1017, Aug. 1994.

[9] H. Ritchie. Semi-Lagrangian advection on a Gaussian grid. *Mon. Weather Rev.*, 115:608-619, 1987.

[10] J. Schmetz and O. M. Turpeinen. Estimation of the upper tropospheric relative humidity field from METEOSAT water vapor image data. *J. Applied Meteorol.*, 27:889-8989, 1988.

[11] S. D. Schubert, R. B. Rood, and J. Pfaendtner. An assimilated dataset for earth science applications. *Bull. Am. Meteorol. Soc.*, 74(12):2331–2342, Dec. 1993.

A   Required forms

The required Report Documentation Pages (NASA Form 1626 and Standard Form 298) are attached.

NASA
National Aeronautics and Space Administration

Report Documentation Page

1. Report No.	2. Government Accession No.	3. Recipient's Catalog No.

4. Title and Subtitle

Distortion Representation of Forecast Errors for Model Skill Assessment and Objective Analysis

5. Report Date

8/15/97

6. Performing Organization Code

7. Author(s)

Ross N. Hoffman, Thomas Nehrkorn and Christopher Grassotti

8. Performing Organization Report No.

P599

10. Work Unit No.

9. Performing Organization Name and Address

Atmospheric and Environmental Research, Inc.
840 Memorial Drive
Cambridge, MA 02139

11. Contract or Grant No.

NAS5-32953

12. Sponsoring Agency Name and Address

NASA/GSFC
Earth Science Procurement Office
Greenbelt, MD 20771

13. Type of Report and Period Covered

Tech. Report 8/15/97

14. Sponsoring Agency Code

15. Supplementary Notes

16. Abstract

We proposed a novel characterization of errors for numerical weather predictions. A general distortion representation allows for the displacement and amplification or bias correction of forecast anomalies. Since we require that these distortion fields vary smoothly, a spectral representation is appropriate. Determining the distortion is equivalent to minimizing the misfit between the verification and a distortion of the forecast, with respect to the spectral coefficients of the distortion. In the present project we use a hemispheric domain, and spherical harmonics as basis functions.

Characterizing and decomposing forecast error is important both for assessing forecast skill and for objective analysis. In this project we focus on the assessment application, restricted to a realistic but univariate 2-dimensional situation. Specifically we study the forecast errors of the sea level pressure and 500 hPa geopotential height fields for forecasts of the short and medium range. Our results show that the methodology works, that a large part of the total error may be explained by a distortion limited to triangular truncation at wavenumber 10, and that the remaining residual error contains mostly small spatial scales.

17. Key Words (Suggested by Author(s))

Numerical Weather Prediction
Forecast Errors

18. Distribution Statement

Unlimited

19. Security Classif. (of this report)	20. Security Classif. (of this page)	21. No. of pages	22. Price
Unclassified	Unclassified		

NASA FORM 1626 OCT 86

PREPARATION OF THE REPORT DOCUMENTATION PAGE

The last page of a report facing the third cover is the Report Documentation Page, RDP. Information presented on this page is used in announcing and cataloging reports as well as preparing the cover and title page. Thus it is important that the information be correct. Instructions for filling in each block of the form are as follows:

Block 1. Report No. NASA report series number, if preassigned.

Block 2. Government Accession No. Leave blank.

Block 3. Recipient's Catalog No. Reserved for use by each report recipient.

Block 4. Title and Subtitle. Typed in caps and lower case with dash or period separating subtitle from title.

Block 5. Report Date. Approximate month and year the report will be published.

Block 6. Performing Organization Code. Leave blank.

Block 7. Author(s). Provide full names exactly as they are to appear on the title page. If applicable, the word editor should follow a name.

Block 8. Performing Organization Report No. NASA installation report control number and, if desired, the non-NASA performing organization report control number.

Block 9. Performing Organization Name and Address. Provide affiliation (NASA program office, NASA installation, or contractor name) of authors.

Block 10. Work Unit No. Provide Research and Technology Objectives and Plans (RTOP) number.

Block 11. Contract or Grant No. Provide when applicable.

Block 12. Sponsoring Agency Name and Address. National Aeronautics and Space Administration, Washington, D.C. 20546-0001. If contractor report, add NASA installation or HQ program office.

Block 13. Type of Report and Period Covered. NASA formal report series; for Contractor Report also list type (interim, final) and period covered when applicable.

Block 14. Sponsoring Agency Code. Leave blank.

Block 15. Supplementary Notes. Information not included elsewhere: affiliation of authors if additional space is re-quired for block 9, notice of work sponsored by another agency, monitor of contract, information about supplements (film, data tapes, etc.), meeting site and date for presented papers, journal to which an article has been submitted, note of a report made from a thesis, appendix by author other than shown in block 7.

Block 16. Abstract. The abstract should be informative rather than descriptive and should state the objectives of the investigation, the methods employed (e.g., simulation, experiment, or remote sensing), the results obtained, and the conclusions reached.

Block 17. Key Words. Identifying words or phrases to be used in cataloging the report.

Block 18. Distribution Statement. Indicate whether report is available to public or not. If not to be controlled, use "Unclassified-Unlimited." If controlled availability is required, list the category approved on the Document Availability Authorization Form (see NHB 2200.2, Form FF427). Also specify subject category (see "Table of Contents" in a current issue of STAR), in which report is to be distributed.

Block 19. Security Classification (of this report). Self-explanatory.

Block 20. Security Classification (of this page). Self-explanatory.

Block 21. No. of Pages. Count front matter pages beginning with iii, text pages including internal blank pages, and the RDP, but not the title page or the back of the title page.

Block 22. Price Code. If block 18 shows "Unclassified-Unlimited," provide the NTIS price code (see "NTIS Price Schedules" in a current issue of STAR) and at the bottom of the form add either "For sale by the National Technical Information Service, Springfield, VA 22161-2171" or "For sale by the Superintendent of Documents, U.S. Government Printing Office, Washington, DC 20402-0001," whichever is appropriate.